Supporting Information for "Nucleation and arrest of fluid-induced aseismic slip"

Antoine B. Jacquey[1]and Robert C. Viesca[1]

[1]Department of Civil and Environmental Engineering, Tufts University, Medford, MA 02155, USA.

Contents of this file

1. Text S1 to S7
2. Figures S1 to S5
3. Table S1

Introduction

This document contains supporting information on the problem formulation and numerical implementation relevant to the numerical results on fluid-induced seismicity presented in the main article entitled "Nucleation and arrest of fluid-induced aseismic slip". In Text S1, we present the semi-analytical solutions for fluid pressure distribution and evolution during and after injection. Text S2 describes the derivation and discretization of the governing equations for fault slip and opening using the Displacement Discontinuity Method

Corresponding author: A. B. Jacquey, Department of Civil and Environmental Engineering, Tufts University, Medford, MA 02155, USA. (antoine.jacquey@tufts.edu)

(derived from the Boundary Element Method). Text S3 presents the elasto-plastic procedure adopted to account for frictional constraints on the fault plane. Text S4 describes the residuals considered in the numerical simulator and the general solution procedure. Text S5 presents a validation of the numerical implementation by comparing the results with a semi-analytical solution. Text S6 introduces Figure S2 showing how the peak slip rate evolves over time after injection shut-in. Text S7 justifies the use of oedometric conditions for the elastic opening of the fault layer in response to fluid pressure change using a procedure similar to (Marck et al., 2015). This paragraph also introduces Figures S4 and S5.

Text S1: fluid pressure during and after injection

Fluid pressure is governed by diffusion along the planar fault interface. For a two-dimensional model, fluid pressure is then governed by the following one-dimensional equation:

$$\frac{\partial p}{\partial t} - \alpha \frac{\partial^2 p}{\partial x^2} = 0, \tag{1}$$

where α is the hydraulic diffusivity and x is the direction of the fault interface. Injection is modeled using a constant pressure fluid source at the origin ($x = 0$). With the following initial and boundary conditions:

$$p\left(x, t = 0\right) = p_0, \quad p\left(x = 0, t > 0\right) = p_0 + \Delta p, \tag{2}$$

the known solution for the fluid pressure is:

$$p\left(x,t\right) = p_0 + \Delta p \ \mathrm{erfc}\left(\frac{|x|}{\sqrt{\alpha' t}}\right), \tag{3}$$

where $\alpha' = 4\alpha$ is the nominal hydraulic diffusivity. After injection shut-in (for $t > t_p$), the fluid pressure is free to diffuse and is subject to the following initial conditions (at the end of the pressurization phase):

$$p\left(x,t=t_p\right) = p_0 + \Delta p \ \mathrm{erfc}\left(\frac{|x|}{\sqrt{\alpha' t_p}}\right). \tag{4}$$

The fluid pressure after injection shut-in can be estimated as the convolution with respect to the spatial variable x of the pressure distribution at $t = t_p$ (Equation 4) and the Green's function (see similar approach by Ciardo and Rinaldi (2022)):

$$p\left(x,t>t_p\right) = p_0 + \frac{\Delta p}{\sqrt{\pi\alpha'\left(t-t_p\right)}} \int_{-\infty}^{+\infty} \mathrm{erfc}\left(\frac{|s|}{\sqrt{\alpha' t_p}}\right) \exp\left(-\frac{|x-s|^2}{\alpha'\left(t-t_p\right)}\right) ds. \tag{5}$$

The convolution in Equation 5 is evaluated numerically using adaptive Gauss-Kronrod quadrature.

Text S2: displacement discontinuity method

For a one-dimensional fault interface, the quasi-static force balance gives the distribution of the normal σ and shear stresses τ respectively as functions of the slip and opening distributions (e.g. Rice et al., 1968):

$$\sigma\left(x,t\right) = \sigma_0 + \frac{\mu'}{\pi} \int_{-a(t)}^{+a(t)} \frac{\partial\phi}{\partial s} \frac{1}{s-x} ds, \tag{6a}$$

$$\tau\left(x,t\right) = \tau_0 + \frac{\mu'}{\pi} \int_{-a(t)}^{+a(t)} \frac{\partial\delta}{\partial s} \frac{1}{s-x} ds, \tag{6b}$$

where ϕ and δ are the fault opening and slip, μ' the effective shear modulus and a the extent of the rupture zone. As we consider a single fault in this study, and because the slip and opening are by definition zero outside the rupture zone, the integrals in equations 6a and 6b can be evaluated on an arbitrary domain size larger than the rupture size ($L > a$). We discretize the fault segment into n elements and make use of piecewise constant shape functions (e.g. Uenishi & Rice, 2003) to approximate the opening and slip distributions:

$$\phi\left(x,t\right) = \sum_{i=1}^{n} \phi_i\left(t\right) \varphi_i\left(x\right), \tag{7a}$$

$$\delta\left(x,t\right) = \sum_{i=1}^{n} \delta_i\left(t\right) \varphi_i\left(x\right). \tag{7b}$$

where ϕ_i and δ_i are the discretized values of opening and slip and φ_i the shape function in the i^{th} element. For one-dimensional elements, piecewise constant shape functions are expressed as:

$$\varphi_i\left(x\right) = H\left(x - x_i\right) - H\left(x - x_{i+1}\right), \tag{8}$$

where H is the Heaviside step function and x_i and x_{i+1} the limit coordinates of the i^{th} element. Replacing the integral over the entire domain into a sum of integrals over each element, leads to the discretized version of Equations 6a and 6b:

$$\sigma_i = \sigma_0 + \sum_{j=1}^{n} \mathbb{E}_{ij}\phi_j, \tag{9a}$$

$$\tau_i = \tau_0 + \sum_{j=1}^{n} \mathbb{E}_{ij}\delta_j. \tag{9b}$$

$\mathbb{E}_{ij}$ is the elastic collocation matrix expressed as:

$$\mathbb{E}_{ij} = \frac{2\mu' a_j}{\pi\left(\left(\bar{x}_i - \bar{x}_j\right)^2 - a_j^2\right)}, \tag{10}$$

where $a_j = \frac{\Delta x_j}{2}$ is the j^{th} element half-length and $\bar{x}_i$ the coordinate of the i^{th} element centroid. In our implementation (see Text S4), we consider Equations 9 in an incremental form (over a fixed time step) to compute the increments of normal and shear stresses ($\Delta\sigma$ and $\Delta\tau$) as functions of the increments of opening and slip ($\Delta\phi$ and $\Delta\delta$) respectively:

$$\Delta\sigma_i = \sum_{j=1}^{n} \mathbb{E}_{ij}\Delta\phi_j, \tag{11a}$$

$$\Delta\tau_i = \sum_{j=1}^{n} \mathbb{E}_{ij}\Delta\delta_j. \tag{11b}$$

Text S3: frictional constraints and elasto-plastic approach

As our model aims at understanding the evolution and distribution of stable aseismic slip, we consider a Mohr-Coulomb frictional strength with constant friction coefficient f formulated here as a plastic yield function noted $\mathcal{F}$:

$$\mathcal{F} = \tau - f\left(\sigma - p\right) \leqslant 0. \tag{12}$$

To account for the constraints imposed by the frictional strength of the fault interface described by Equation 12, we rely on an elasto-plastic splitting for the stress update. We consider the fault surface to be the boundaries of a layer of thickness h. Fault slip and opening are understood to be the difference in displacement between the top and bottom of this layer (see Figure S1). The fault layer can undergo elastic and plastic deformation

in response to a given shear and normal stress. The deformation within the layer is described by homogeneous normal and shear strain. Assuming an additive splitting of the shear strain into elastic and plastic parts, the local stress increments at a point along the fault surface can be given as:

$$\Delta\sigma - \alpha_B \Delta p = \kappa \frac{\Delta\phi}{h}, \tag{13a}$$

$$\Delta\tau = \mu \left(\frac{\Delta\delta}{h} - \Delta\gamma^p \right), \tag{13b}$$

where κ is the normal modulus, α_B is the Biot's poroelastic coefficient, $\Delta\gamma = \frac{\Delta\delta}{h}$ the total shear strain increment, and $\Delta\gamma^p$ the plastic shear strain increment. Equations 13 give a local stress update based on the relative displacement across the layer. Equations 13 describe oedometric deformation conditions which are valid when the diffusion length scale is large compared to the fault thickness ($\sqrt{\alpha' t} \gg h$). We discuss the validity of this approximation and the expression of the normal modulus κ in Text S7. The plastic strain is updated following a non-associative (zero dilation) flow rule resulting in plastic deformation only in the shear direction.

The plastic update is done in three steps: (i) first the trial shear stress is computed for a given time step, (ii) the trial yield condition is computed based on the trial shear stress and normal effective pressure, and (iii) the trial shear stress is corrected if yielding occurs. For the k^{th} time step (quantities with subscript (k)), the trial shear stress τ^{tr} is given as:

$$\tau^{tr}_{(k)} = \tau_{(k-1)} + \mu \Delta\gamma_{(k)}, \tag{14}$$

where $\Delta\gamma_{(k)} = \frac{\Delta\delta_{(k)}}{h}$ is the increment of total shear strain for this time step. With this definition, we can also express the plastic correction from the trial state to obtain the final shear stress when plastic deformation occurs:

$$\tau_{(k)} = \tau^{tr}_{(k)} - \mu\Delta\gamma^{p}_{(k)}. \tag{15}$$

The increment of plastic strain is obtained by combining Equations 15 and 12 together as:

$$\Delta\gamma^{p}_{(k)} = \begin{cases} 0, & \text{if } \tau^{tr}_{(k)} - f\sigma'_{(k)} < 0, \\ \frac{\tau^{tr}_{(k)} - f\sigma'_{(k)}}{\mu}, & \text{otherwise.} \end{cases} \tag{16}$$

Text S4: update procedure

For each time step, we solve for the increments of slip $\Delta\delta$ and of opening $\Delta\phi$ given the change in fluid pressure along each element, Δp. The equations governing the increments follow from the combination of Equations 11 and 13:

$$\begin{aligned} \sum_{j=1}^{n} \mathbb{E}_{ij}\Delta\phi_j - \frac{\kappa}{h}\Delta\phi_i - \alpha_B\Delta p_i = 0, \\ \sum_{j=1}^{n} \mathbb{E}_{ij}\Delta\delta_j - \frac{\mu}{h}\left(\Delta\delta_i - h\Delta\gamma^{p}_{i}\right) = 0, \end{aligned} \tag{17a}$$

where the subscript i indicates the position of the i^{th} element in the mesh. We denote the left-hand side of these equations the normal and shear residuals, $R_{\phi,i}\left(\Delta\phi_i\right)$ and $R_{\delta,i}\left(\Delta\phi_i, \Delta\delta_i\right)$ respectively. The opening ϕ is governed by elastic deformation within the fault induced by changes in fluid pressure and the slip δ is governed by frictional

constraints. Where plastic deformation occurs, the shear residuals depend both on the increments of opening and of slip as Equation 16 can be alternatively expressed when plastic deformation occurs as:

$$\Delta\gamma^p_{(k)} = \frac{\tau_{(k-1)} - f\left(\sigma - p_{(k-1)}\right)}{\mu} + \frac{\Delta\delta_{(k)}}{h} - \frac{f}{\alpha_B}\frac{\kappa}{\mu}\frac{\Delta\phi_{(k)}}{h}. \tag{18}$$

Equations 17 are solved for using Newton-Raphson iterations and a BiCGstab(l) iterative linear solver. The normal effective stress and shear stress are also updated at the end of each time step. At the beginning of each time step, the increments of opening and slip are initialized to zero, and we compute the changes in fluid pressure using the expressions from Text S1. During the first evaluation of the residuals, the shear residuals are equal to zero as the increment of slip is zero and the normal residuals nonzero due to the changes in fluid pressure. In a second iteration, the changes in opening induced by the fluid pressure changes will trigger changes in normal effective stress and therefore plastic deformation where yielding occurs. This, in turn, induces slip on the fault plane. The Newton-Raphson iterations are stopped when the norm of the residuals reaches or is smaller than a given absolute tolerance (1.0×10^{-12} by default). After a successful solve, the cumulative values of opening, slip, normal stress, and shear stress are updated based on the computed increments.

Text S5: verification of the implementation

The implementation of the displacement discontinuity method together with the elasto-plastic correction for frictional constraints have been verified against the analytical solu-

tion provided by Viesca (2021) for aseismic slip in response to a constant pressure fluid source.

Figure S2 shows the comparison between the analytical solution of Viesca (2021) and the numerical solution obtained with 10 000 elements. These results were obtained considering a fault stress parameter $T = \left(1 - \frac{\tau_0}{f\sigma_0'}\right) \frac{\sigma_0'}{\Delta p} = 0.5$. The full list of parameter values can be found in Table S1.

Text S6: peak slip rate evolution after injection shut-in

The maximum slip rate after injection shut-in decays over time until becoming null at the arrest time. We demonstrated in the accompanied manuscript that the final arrest time is proportional to the pressurization duration. Here we also show that the peak slip rate scales with the inverse of the square root of the pressurization duration. Furthermore, the evolution of the scaled slip rate is self-similar on time as depicted in Figure S3 as results for three different pressurization durations collapse into one line. However, the slip rate is not self-similar over space in general after injection shut-in.

Text S7: conditions of oedometric conditions for elastic opening in response to a change in fluid pressure

The constitutive relation for the deformation of a linear poroelastic medium is given in an incremental form by (Rice & Cleary, 1976; Cheng & Detournay, 1988):

$$\Delta\boldsymbol{\sigma}_{ij} = 2\mu\Delta\boldsymbol{\varepsilon}_{ij} + \lambda\Delta\varepsilon_{kk}\delta_{ij} - \alpha_B\Delta p\delta_{ij}, \tag{19}$$

where $\boldsymbol{\varepsilon}_{ij}$ is the strain tensor, λ and μ the first and second (shear) Lamé moduli and α_B the Biot's poroelastic coefficient. The change in normal stress $\Delta\sigma = -\boldsymbol{n}_i \Delta\boldsymbol{\sigma}_{ij}\boldsymbol{n}_j$ can be expressed as a function of the normal strain $\Delta\epsilon = -\boldsymbol{n}_i \Delta\boldsymbol{\varepsilon}_{ij}\boldsymbol{n}_j$ as:

$$\Delta\sigma - \alpha_B \Delta p = 2\mu\Delta\epsilon - \lambda\Delta\varepsilon_{kk}, \tag{20}$$

with $\boldsymbol{n}$ being the normal vector to the fault plane. The increment in volumetric strain can be decomposed into a normal and tangential parts, leading to:

$$\Delta\sigma - \alpha_B \Delta p = (\lambda + 2\mu)\,\Delta\epsilon - \lambda\Delta\varepsilon_{xx}, \tag{21}$$

for a horizontal fault plane in a two-dimensional setting with x being the horizontal coordinate, as described in our model. Marck et al. (2015) showed that, for a vertical line source injecting fluid at constant injection rate in a finite thickness fault surrounded by impermeable and elastic semi-infinite domains for axisymmetric geometries, the deformation rate of vertical displacement becomes oedometric (uniaxial) when the diffusion radius is large compared to the fault layer thickness. In the following, we demonstrate that this is also true in two dimensions for a line source injecting fluid at constant pressure as considered in this study and that, under such conditions, the first term of the left-end side ($\Delta\sigma$) and the second term on the right-end side ($-\lambda\Delta\varepsilon_{xx}$) of Equation 21 can be neglected. To that end, we use a similar procedure as the one introduced from Marck et al. (2015).

Figure S4 shows the geometry of the model consisting in a line source injecting fluid within a finite thickness poroelastic layer at constant pressure. While the pressure within

the poroelastic layer is given by Equation 1, it can be extended to the impermeable domains as:

$$p\left(x,z,t\right) = p_x\left(x,t\right) L\left(z\right), \tag{22}$$

with p_x being the solution given by Equation 1 (independent of z) and $L\left(z\right) = \left[H\left(z+\frac{h}{2}\right) - H\left(z-\frac{h}{2}\right)\right]$ with H being the heaviside step function. The displacement vector $\boldsymbol{u}$ within the poroelastic layer is governed by the following equation, assuming an irrotational displacement field (Marck et al., 2015):

$$\nabla^2 \boldsymbol{u} = \frac{\eta}{\mu} \nabla p, \tag{23}$$

with $\eta = \frac{\alpha_B(1-2\nu)}{2(1-\nu)}$ being the poroelastic stress coefficient with $0 \leqslant \eta \leqslant \frac{1}{2}$.

Introducing the following scaling and dimensionless quantities:

$$\xi = \frac{x}{h}, \quad \zeta = \frac{z}{h}, \quad \tau = \frac{\alpha'}{t^2}, \quad P = \frac{p-p_0}{\Delta p}, \quad \boldsymbol{U} = \frac{\boldsymbol{u}}{\beta h}, \tag{24}$$

where $\alpha' = 4\alpha$ and $\beta = \frac{\eta \Delta p}{\mu}$, Equations 23 and 22 can be rewritten as:

$$\frac{\partial U_\xi}{\partial \xi^2} + \frac{\partial U_\xi}{\partial \zeta^2} = \frac{\partial P_\xi}{\partial \xi} \, L\left(\zeta\right), \tag{25a}$$

$$\frac{\partial U_\zeta}{\partial \xi^2} + \frac{\partial U_\zeta}{\partial \zeta^2} = P_\xi \, \frac{dL}{d\zeta}\left(\zeta\right), \tag{25b}$$

$$P_\xi\left(\xi,\tau\right) = \operatorname{erfc}\left(\frac{|\xi|}{\sqrt{\tau}}\right), \tag{25c}$$

with $L\left(\zeta\right) = H\left(\zeta+\frac{1}{2}\right) - H\left(\zeta-\frac{1}{2}\right)$ and $\frac{dL}{d\zeta}\left(\zeta\right) = \delta_D\left(\zeta+\frac{1}{2}\right) - \delta_D\left(\zeta-\frac{1}{2}\right)$, δ_D being the Dirac delta function. The solutions for the horizontal and vertical displacements (U_ξ and U_ζ respectively) can be found using the sine and cosine Fourier transforms given by:

$$\mathcal{F}_{\sin}\left[f\left(t\right)\right]\left(\omega\right) = \sqrt{\frac{2}{\pi}}\int_0^{+\infty} f\left(t\right)\sin\left(\omega t\right)dt, \tag{26a}$$

$$\mathcal{F}_{\cos}\left[f\left(t\right)\right]\left(\omega\right) = \sqrt{\frac{2}{\pi}}\int_0^{+\infty} f\left(t\right)\cos\left(\omega t\right)dt, \tag{26b}$$

together with their inverse transforms:

$$\mathcal{F}_{\sin}^{-1}\left[F\left(t\right)\right]\left(\omega\right) = \sqrt{\frac{2}{\pi}}\int_0^{+\infty} F\left(\omega\right)\sin\left(\omega t\right)d\omega, \tag{27a}$$

$$\mathcal{F}_{\cos}^{-1}\left[F\left(t\right)\right]\left(\omega\right) = \sqrt{\frac{2}{\pi}}\int_0^{+\infty} F\left(\omega\right)\cos\left(\omega t\right)d\omega. \tag{27b}$$

Because of the symmetry of U_ζ and anti-symmetry of U_ξ with respect to the plane $\xi = 0$ and because of the symmetry of U_ξ and the anti-symmetry of U_ζ with respect to the plane $\zeta = 0$, we obtain the following solutions for the transformed fields $\overline{U}_\xi$ and $\overline{U}_\zeta$:

$$\overline{U}_\xi\left(\chi,\omega\right) = \mathcal{F}_{\cos}\left[\mathcal{F}_{\sin}\left[U_\xi\left(\xi,\zeta\right)\right]\left(\chi,\zeta\right)\right]\left(\chi,\omega\right) = \frac{4}{\pi^{3/2}\left(\chi^2+\omega^2\right)}\mathrm{F}\left(\frac{\chi\sqrt{\tau}}{2}\right)\frac{\sin\left(\frac{\omega}{2}\right)}{\omega}, \tag{28a}$$

$$\overline{U}_\zeta\left(\chi,\omega\right) = \mathcal{F}_{\sin}\left[\mathcal{F}_{\cos}\left[U_\zeta\left(\xi,\zeta\right)\right]\left(\chi,\zeta\right)\right]\left(\chi,\omega\right) = \frac{4}{\pi^{3/2}\left(\chi^2+\omega^2\right)}\frac{\mathrm{F}\left(\frac{\chi\sqrt{\tau}}{2}\right)}{\chi}\sin\left(\frac{\omega}{2}\right), \tag{28b}$$

with $\mathrm{F}\left(x\right) = e^{-x^2}\int_0^{+\infty} e^{t^2}dt$ is the Dawson function. The inversion of the Fourier transform with respect to the variable ω can be performed directly to obtain the transforms (with respect to ξ) of the horizontal displacement in the center of the layer $\widetilde{U}_\xi\left(\chi,\zeta=0\right)$ and of the vertical displacement at the top of the layer $\widetilde{U}_\zeta\left(\chi,\zeta=\frac{1}{2}\right)$:

$$\widetilde{U}_\xi\left(\chi,\zeta=0\right) = \mathcal{F}_{\sin}\left[U_\xi\left(\xi,\zeta\right)\right]\left(\chi,\zeta\right) = \frac{2\sqrt{2}}{\pi}\frac{\mathrm{F}\left(\frac{\chi\sqrt{\tau}}{2}\right)}{\chi^2}\left(1-e^{-\left|\frac{\chi}{2}\right|}\right), \tag{29a}$$

$$\widetilde{U}_\zeta\left(\chi,\zeta=1\right) = \mathcal{F}_{\cos}\left[U_\zeta\left(\xi,\zeta\right)\right]\left(\chi,\zeta\right) = \frac{\sqrt{2}}{\pi}\frac{\mathrm{F}\left(\frac{\chi\sqrt{\tau}}{2}\right)}{\chi^2}\left(1-e^{-|\chi|}\right). \tag{29b}$$

The inverse transforms with respect to χ are evaluated numerically and the final solutions for $U_\xi\left(\xi, \zeta = 0\right)$ and $U_\zeta\left(\xi, \zeta = \frac{1}{2}\right)$ are displayed in Figure S5 as functions of ξ and evaluated at different times τ.

Figure S5 demonstrates that the vertical displacement solution (correspond to half of opening) becomes similar to the fluid pressure solution at large time scales ($\tau > 10^4$), which corresponds to the diffusion length scale being larger than the fault thickness ($\sqrt{\alpha' t} \gg h$). This regime corresponds to oedometric or uniaxial normal deformation of the poroelastic layer in response to a change in fluid pressure. At large times, the maximum value of the horizontal displacement reaches a plateau and spans larger distances (note the *log*-scale of ξ in Figure S5-(a)), thus demonstrating the decay of the horizontal strain ε_{xx} and of change in normal stress over time. In conclusion, when the diffusion scale becomes large compare to the fault thickness, the first term of the left-end side and the second term of the right-end side of Equation 21 can be neglected and simplifies to a simple relation between change in fluid pressure and change in opening. With the values of the physical properties considered in this study and summarized in Table S1, oedometric conditions are reached after $t >$0.25 s of injection. After injection shut-in, the fluid pressure gradient decreases significantly with time which ensures that oedometric conditions are still valid. With this approximation, with Equation 21 simplifies to:

$$\alpha_B \Delta p = -\left(\lambda + 2\mu\right) \Delta\epsilon = -\kappa \frac{\Delta\phi}{h}, \tag{30}$$

where $\Delta\epsilon = \frac{\Delta\phi}{h}$ and $\kappa = \lambda + 2\mu = \frac{\alpha_B \mu}{\eta}$.

References

Cheng, A. H., & Detournay, E. (1988). A direct boundary element method for plane strain poroelasticity. *International Journal for Numerical and Analytical Methods in Geomechanics*, *12*(5), 551–572. doi: 10.1002/nag.1610120508

Ciardo, F., & Rinaldi, A. P. (2022). Impact of injection rate ramp-up on nucleation and arrest of dynamic fault slip. *Geomechanics and Geophysics for Geo-Energy and Geo-Resources*, *8*(1), 28. doi: 10.1007/s40948-021-00336-4

Marck, J., Savitski, A. A., & Detournay, E. (2015). Line source in a poroelastic layer bounded by an elastic space: Line source in a poroelastic layer bounded by an elastic space. *International Journal for Numerical and Analytical Methods in Geomechanics*, *39*(14), 1484–1505. doi: 10.1002/nag.2405

Rice, J. R., & Cleary, M. P. (1976). Some basic stress diffusion solutions for fluid-saturated elastic porous media with compressible constituents. *Reviews of Geophysics*, *14*(2), 227–241. doi: 10.1029/rg014i002p00227

Rice, J. R., et al. (1968). Mathematical analysis in the mechanics of fracture. *Fracture: an advanced treatise*, *2*, 191–311.

Uenishi, K., & Rice, J. R. (2003). Universal nucleation length for slip-weakening rupture instability under nonuniform fault loading. *Journal of Geophysical Research: Solid Earth (1978–2012)*, *108*(B1). doi: 10.1029/2001jb001681

Viesca, R. C. (2021). Self-similar fault slip in response to fluid injection. *Journal of Fluid Mechanics*, *928*, A29. doi: 10.1017/jfm.2021.825

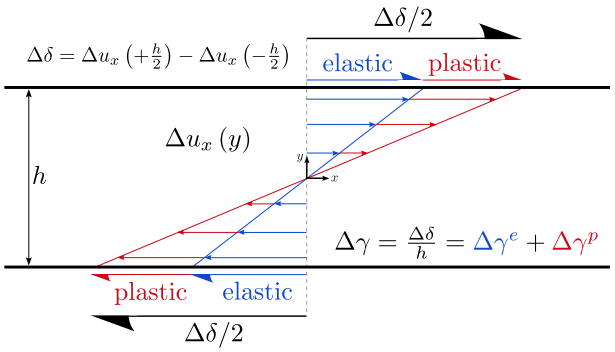

Figure S1. Physical representation of the elasto-plastic splitting of fault shear strain. Slip is defined as the difference in horizontal displacement between the top and bottom of a fault layer of thickness h. The homogeneous shear strain within the layer is split additively into elastic and plastic parts. The magnitude of the elastic strain increment (compared to the plastic one) has been greatly amplified for visual purpose.

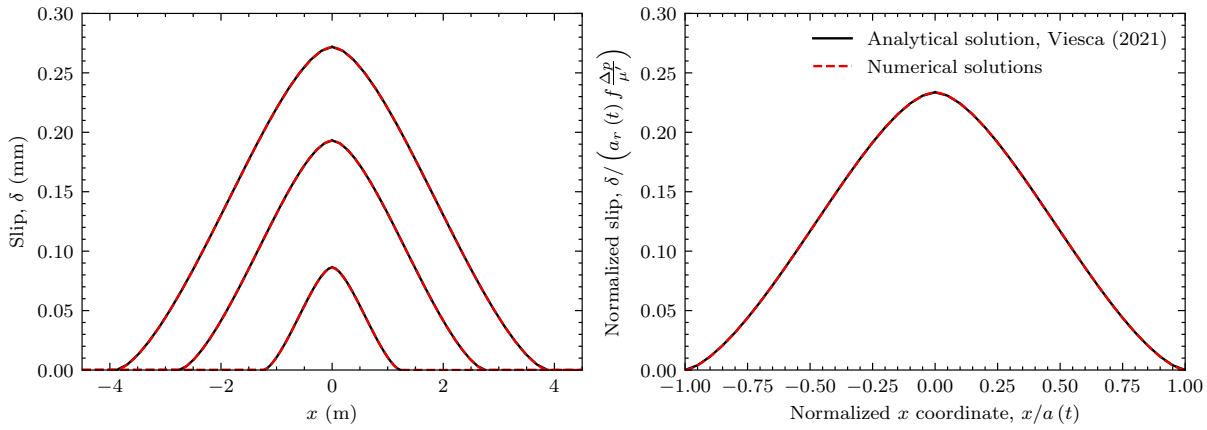

Figure S2. Slip profiles after 1, 5, and 10 mins of pressurization (left) and in its dimensionless form (right) compared with the analytical solution from Viesca (2021).

Table S1. Parameter list for the simulations.

Parameter	Value	Unit
μ'	20	GPa
ν	0.3	–
h	1	mm
σ_0	50	MPa
p_0	20	MPa
σ'_0	30	MPa
f	0.5	–
Δp	12	MPa
α	0.01	$\mathrm{m\,s^{-2}}$
α'	0.04	$\mathrm{m\,s^{-2}}$

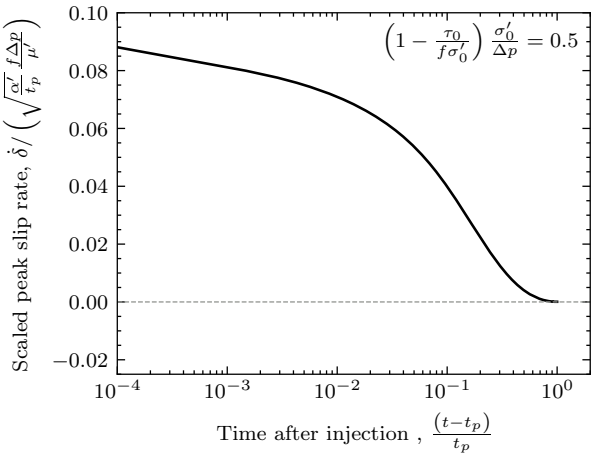

Figure S3. Evolution of the scaled peak slip rate after injection shut-in for three different pressurization durations (collapsed in a single line).

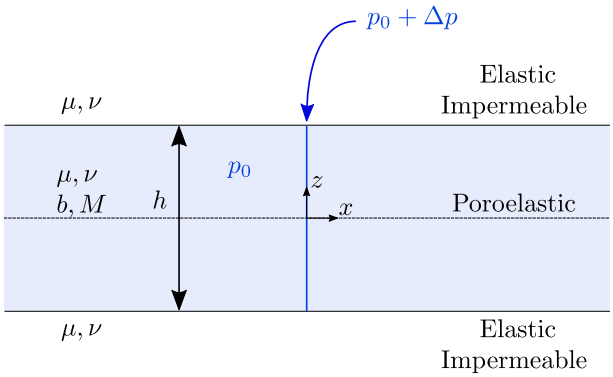

Figure S4. A line source injecting fluid at constant pressure within a poroelastic fault layer surrounded by elastic and impermeable semi-infinite domains.

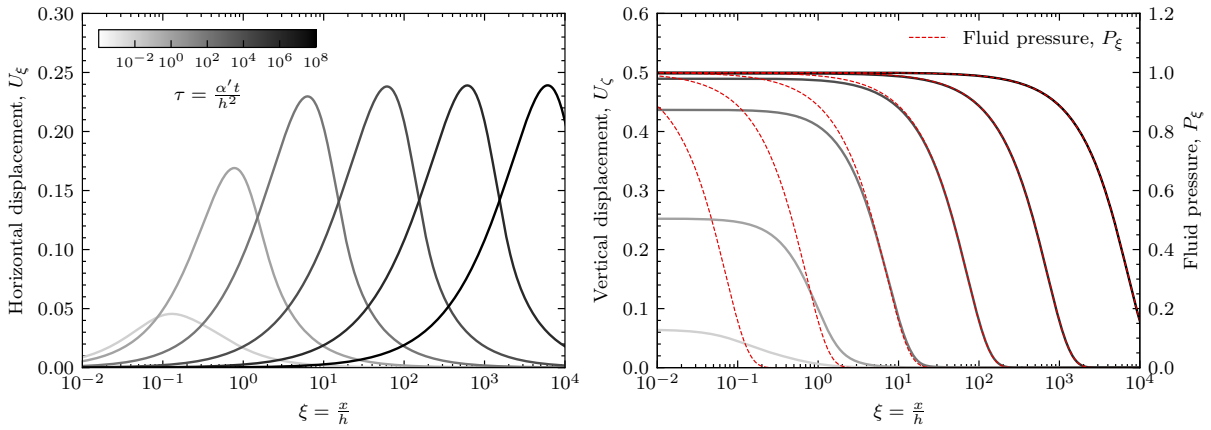

Figure S5. Solutions for (left) the horizontal displacement U_ξ evaluated at $\zeta = 0$ and for (right) the vertical displacement U_ζ evaluated at $\zeta = \frac{1}{2}$ at different times τ indicated by the ticks of the color bar. The red dashed lines in (b) corresponds to the fluid pressure solutions.